The Quadrature Signals Synchronous Demodulation Method for Rotor Position Estimation of Three-Stage Synchronous Machine

Jiadan Wei, *Senior Member, IEEE*, Zhengyou Cai, *Graduate Student Member, IEEE*, Le Zhang, Junhao Yu, *Student Member, IEEE*, Zhuoran Zhang, *Senior Member, IEEE*, and Bo Zhou

***Abstract*—In this article, based on the analysis of the rotor position estimation error caused by the asynchronous demodulation method and the low-pass filter (LPF), a novel quadrature signals synchronous demodulation method without the LPF is proposed for the sensorless starting control of the three-stage synchronous machine (TSSM). The second harmonic voltage caused by the rotating rectifier is employed as the high-frequency (HF) signal injected into the field winding of the main generator (MG). The cascade filter composed of the comb filter and the second-order generalized integrators (SOGI) is proposed to extract the HF response signals containing rotor position information and generate the quadrature signals simultaneously for rotor position estimation. Then, the synchronous demodulation method could be simplified to obtain the estimated rotor position with higher accuracy and reliability. Finally, the effectiveness of the proposed method is verified by the simulation and experiment results.**

***Index Terms*—Cascade filter, quadrature signals synchronous demodulation method, rotor position estimation error, sensorless starting control, three-stage synchronous machine (TSSM).**

I. INTRODUCTION

IN THE development trend of the more electric aircraft for the modern aircraft [1], [2], the high-power integrated starter/generator (ISG) system is the core technology to achieve higher performance for the aircraft power system [3]. The three-stage synchronous machine (TSSM) as shown in Fig. 1 has been widely used in aviation power systems due to the properties of its mature structure and simple voltage regulation [4], [5]. Moreover, it is also the candidate for the ISG based on the four-quadrant operation characteristics.

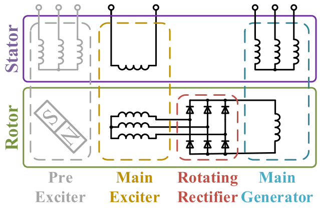

Fig. 1. Structure diagram of TSSM.

As the structure of TSSM shown in Fig. 1, there are four parts connected in coaxial, such as pre-exiter, main exciter (ME), rotating rectifier, and main generator (MG). In the generation mode, the ME and rotating rectifier are employed to achieve brushless excitation for MG. While, in the starting mode, the ME works as the rotating transformer with the ac excitation to provide excitation power for MG, then the MG could be driven to crank the engine. While, the rotor position information of MG is also required for the driving control of MG, and it is not necessary for the generation mode. Thus, the sensorless starting control technology is an effective approach to achieve the integrated starting and generation function of TSSM without any structural changes, such as the coaxially fixed mechanical position sensor, and the property of TSSM for the aircraft could be maintained.

In the traditional rotor position estimation methods for ac machines at the high-speed range, the back electromagnetic force (EMF) of the machine is detected for the rotor position estimation by the approaches of the sliding-mode observer, extended state observer, and so on [6], [7], [8]. Moreover, the Kalman filter and model reference adaptive theory are employed herein to achieve the robustness of the proposed method [9], [10], [11]. In the proposed ISG system based on TSSM, the starting control is required to crank the engine from standstill status to the ignition speed, correspondingly, the rotor position of TSSM must be estimated at the same speed range, while the traditional method based on the EMF is not suitable for the sensorless starting control of TSSM at the standstill status and low-speed range.

As a result, the high-frequency (HF) signal injection (HFSI) method for the rotor position estimation is employed for TSSM at the standstill status and low-speed range. The external HF signal is injected into the windings, and the response HF signal composed of the rotor position information is extracted and

---

Manuscript received 14 August 2023; revised 2 December 2023 and 26 January 2024; accepted 23 February 2024. Date of publication 27 February 2024; date of current version 19 April 2024. This work was supported in part by the National Natural Science Foundation of China under Grant 51877110 and in part by the Qinlan Innovation Project of Jiangsu University under Grant YQR21052. Recommended for publication by Associate Editor A. Gupta. *(Corresponding author: Jiadan Wei.)*

Jiadan Wei, Zhengyou Cai, Junhao Yu, Zhuoran Zhang, and Bo Zhou are with the Department of Electrical Engineering, College of Automation Engineering, Nanjing University of Aeronautics and Astronautics, Nanjing 211106, China (e-mail: weijiadan@nuaa.edu.cn; caizhengyou@nuaa.edu.cn; yujunhao@nuaa.edu.cn; apsc-zzr@nuaa.edu.cn; zhoubo@nuaa.edu.cn).

Le Zhang is with the Department of Automation Engineering, Wuxi Taihu University, Wuxi 214063, China (e-mail: zhangl1@wxu.edu.cn).

Color versions of one or more figures in this article are available at https://doi.org/10.1109/TPEL.2024.3370825.

Digital Object Identifier 10.1109/TPEL.2024.3370825

demodulated to achieve the estimated rotor position [12], [13]. Due to the specific structure of TSSM, the proposed HFSI method could be sorted in two different ways with respect to the signal injection method and the rotor position demodulation method.

Due to the multistage structure of TSSM, the external HF signal can be injected into either the field winding of ME [14], [15], [16] or the armature windings of MG [17], [18], and the corresponding rotor position demodulation methods are also different. Since the signal-to-noise ratio (SNR) of the HF response signal is determined by the amplitude of the externally injected HF signal, it is of great significance to the accuracy of the estimated rotor position. Thus, the amplitude of the external HF signal should be large enough, while the large amplitude of the injected HF signal will lead to the obvious torque fluctuation to deteriorate the output performance of TSSM in the starting procedure, especially when the external HF signal is injected into the armature windings of MG. Therefore, the amplitude of the external HF signal is one of the key issues for the proposed rotor position estimation method for the TSSM. Since the ME and MG of TSSM are coaxially connected, the ME could be employed as the rotor position sensor according to the current and flux characteristics [19], [20], and the additional injected HF signals are eliminated. Furthermore, as the rotating rectifier of TSSM will lead to the high order harmonics in the field winding of the MG, the harmonics could also be used as indirectly injected HF signals to the MG [21], [22], without the additional injected HF signals, the aforementioned issues could be ignored.

As the rotor position information is the low-frequency (LF) component in the HF response signals, a low-pass filter (LPF) is commonly necessary to demodulate the rotor position signals [23]. Moreover, the rotor position information of the LF component is changed arising from the phase-shift with respect to the LPF, especially in the starting process, the frequency of LF signals such as the current and voltage vary according to the speed. With the speed increasing, the frequency of the LF signal increases, and the rotor position estimation error will also increase correspondingly due to the phase-shift compensation of LPF for the response signal, the output performance of TSSM will also deteriorate. In order to deal with the above issues, Wei et al. [24] proposed the second-order generalized integrator (SOGI) to replace the traditional digital filters with the fixed cut-off frequency in the demodulation method, where the phase shift could be significantly reduced. However, there is still a phase shift of SOGI when it is employed as the LPF, and it has a side effect on the accuracy of the estimated rotor position similarly.

Furthermore, in [25], the rotor position error between the actual and estimated rotor position is employed in the demodulation method, where the HF component in the response signals is eliminated by division calculation, and LPF is eliminated correspondingly. However, the distortion with respect to the zero-crossing point of the denominator will reduce the stability of the rotor position estimation method. Wang et al. [26] proposed an auxiliary square wave sampling method to replace the traditional LPF in the demodulation, while the amplitude imbalance of the demodulated LF component will lead to the rotor position estimation error. Although the error can be compensated by the first quadrant definite integral method, the proposed rotor position estimation method is relatively complex.

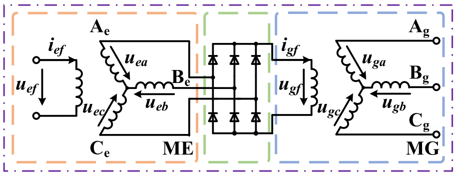

Fig. 2. Schematic diagram of the two-stage structure.

To overcome the aforementioned issues in the rotor position estimation method for the sensorless starting control of TSSM, a novel quadrature signals synchronous demodulation method based on harmonic self-injection without LPF is proposed. The second harmonic voltage caused by the rotating rectifier is employed as an HF signal injected into the field winding of MG so that the external HF signal injection link is eliminated to avoid the torque fluctuation issue.

The rest of this article is organized as follows. In Section II, the principle of harmonic self-injection is analyzed, and the demodulation method based on the heterodyne scheme is introduced. Then, the quadrature signals synchronous demodulation method based on CF cascade SOGI structure is proposed in Section III for the synchronous decoupling signals generation. The simulation and experimental results are implemented to verify the effectiveness of the proposed method in Sections IV and V. Finally, Section VI concludes this article.

II. PRINCIPLE OF SELF-HARMONIC INJECTION AND DEMODULATION SCHEME

A. *Principle of Self-Harmonic Injection Method*

In the starting mode, ME is energized by a single-phase AC power as shown in Fig. 2, where PE is not employed herein, and ME and MG of TSSM work in the two-stage mode, and the excitation current in the field winding of the ME can be expressed as

$$i_{ef} = I_{ef} \sin(\omega_{ex} t + \varphi_{e0}) \tag{1}$$

where ω_{ex} is the frequency of the excitation power for ME, I_{ef} is the amplitude, and φ_{e0} is the initial phase angle.

Then, the back EMF generated in the armature winding of phase A can be expressed as

$$\begin{aligned} e_{ea} &= \frac{d}{dt}(M_{esf} \cos\theta_e \cdot i_{ef}) \\ &= M_{esf} I_{ef} [\omega_{ex} \cos(\omega_{ex} t + \varphi_{e0}) \cos(\omega_{er} t + \theta_{e0}) \\ &\quad - \omega_{er} \sin(\omega_{ex} t + \varphi_{e0}) \sin(\omega_{er} t + \theta_{e0})] \end{aligned} \tag{2}$$

where M_{esf} is the maximum value of the mutual inductance between the field winding and armature windings of ME, $\theta_e = \omega_{er} t + \theta_{e0}$ is the rotor position angle of ME, ω_{er} is the electrical angular frequency of ME, and θ_{e0} is the initial rotor position angle of ME.

Then, the back EMF of the armature windings of ME can be obtained and rectified by the rotating rectifier. With the ignorance

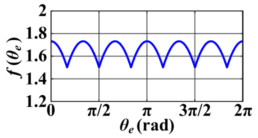

Fig. 3. Schematic curve of $f(\theta_e)$.

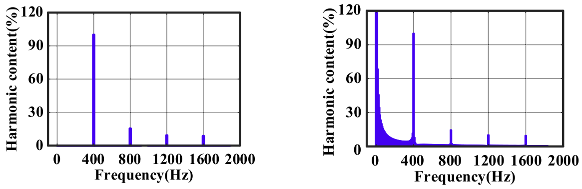

(a)

(b)

Fig. 4. FFT analysis of the back EMF of the armature windings of MG. (a) Stationary state. (b) Rotation state.

of phase change overlap caused by inductance parameters of TSSM, the voltage of the field winding of MG can be expressed as

$$\begin{aligned} u_{gf} &= \max\{|e_{ea}-e_{eb}|, |e_{ea}-e_{ec}|, |e_{eb}-e_{ec}|\} \\ &= E_s\,|\cos(\omega_{ex}t+\varphi_{e0})|\, f(\theta_e) \end{aligned} \tag{3}$$

where e_{eb} and e_{ec} are the back EMF in the armature windings of ME of phase B and phase C respectively, E_s is the amplitude, $f(\theta_e)$ is the coefficient of the amplitude of u_{gf} with respect to the rotor position of ME as shown in Fig. 3.

The HF components in (3) can be decomposed as

$$\begin{aligned} &|\cos(\omega_{ex}t+\varphi_{e0})| \\ &\quad = U_{dc} + \sum_{n=1}^{+\infty} U_{acn}\cos[2n(\omega_{ex}t+\varphi_{e0})], n=0,1,2\cdots \\ &U_{acn} = \frac{4\cdot(-1)^n}{\pi(1-4n^2)}, n=1,2,3\ldots \end{aligned} \tag{4}$$

where U_{dc} is the dc component, U_{acn} is the amplitude of the ac components. It can be seen from (4) that the field voltage of MG is composed of the dc component and even harmonics. As shown in Fig. 4, the even harmonics in the field winding of MG will also generate EMF of the same frequency in the armature windings.

Since the excitation frequency is 200 Hz, the frequency of even harmonics of EMF are multiples of 200 Hz. It can be seen from (4) and Fig. 4 that the second harmonic of EMF has the highest amplitude and SNR, so that the second harmonic is selected to be employed as the self-injected HF signal for the field winding of MG. Then, HF response signals in the $\alpha\beta$-axis of the armature windings of MG can be extracted as follows:

$$\begin{cases} u_{\alpha h} = U_h[2\omega_{ex}\cos(2\omega_{ex}t+\varphi_h)\cos\theta \\ \qquad\quad -\,\omega_r\sin(2\omega_{ex}t+\varphi_h)\sin\theta] \\ u_{\beta h} = U_h[2\omega_{ex}\cos(2\omega_{ex}t+\varphi_h)\sin\theta \\ \qquad\quad +\,\omega_r\sin(2\omega_{ex}t+\varphi_h)\cos\theta] \end{cases} \tag{5}$$

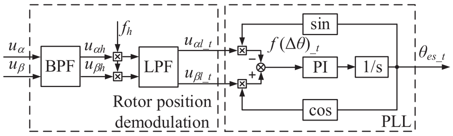

Fig. 5. Schematic diagram of the heterodyne demodulation module.

where U_h is the amplitude of the HF response signals, φ_h is the phase angle, θ is the rotor position of MG, and ω_r is the electrical angular frequency of MG.

It can be seen that the rotor position information of TSSM is composed in (5) in the sine and cosine form, and it needs to be extracted and estimated by the specific demodulation scheme.

B. Heterodyne Demodulation Module

The traditional heterodyne demodulation module for rotor position signal extraction is shown in Fig. 5, which is similar to the method commonly used in the sensorless starting control of permanent magnet synchronous machines (PMSMs). The HF response signals are multiplied with the demodulation signal f_h with the same frequency. Then, the LPF is adopted to extract the LF signals containing the rotor position information by the phase-locked loop (PLL). However, as the phase of the HF response signals is changed during the transmission process in the harmonic self-injection scheme, and the phase between the demodulation signal named f_h and the HF response signals is unknown, which can be expressed as

$$f_h = \cos(2\omega_{ex}t+\varphi_{d\_t}) \tag{6}$$

where φ_{d_t} is the phase of the demodulation signal, and the value could not be confirmed, it should be set according to the rotor position compensation scheme.

Then, the signal input to the LPF can be expressed as

$$\begin{cases} u_{\alpha h}\cdot f_h = \frac{U_h}{2}\{2\omega_{ex}[\cos(4\omega_{ex}t+\varphi_{\text{sum}})+\cos\Delta\varphi_t]\cos\theta \\ \qquad -\omega_r[\sin(4\omega_{ex}t+\varphi_{\text{sum}})+\sin\Delta\varphi_t]\sin\theta\} \\ u_{\beta h}\cdot f_h = \frac{U_h}{2}\{2\omega_{ex}[\cos(4\omega_{ex}t+\varphi_{\text{sum}})+\cos\Delta\varphi_t]\sin\theta \\ \qquad +\omega_r[\sin(4\omega_{ex}t+\varphi_{\text{sum}})+\sin\Delta\varphi_t]\cos\theta\} \end{cases} \tag{7}$$

where $\varphi_{\text{sum}} = \varphi_h + \varphi_{d\_t}$ is the phase sum of the HF response signals and the demodulation signal, $\Delta\varphi_t = \varphi_h - \varphi_{d\_t}$ is the phase difference.

Since the HF component in (7) is suppressed by the LPF, the phase-shift rising with the increasing of rotational speed in the starting procedure is also introduced into the LF component. The extracted LF signals with the consideration of the phase shift caused by the LPF can be expressed as

$$\begin{cases} u_{\alpha l\_t} = \frac{U_h}{2}[2\omega_{ex}\cos\Delta\varphi_t\cos(\theta+\varphi_{\text{LPF}}) \\ \qquad -\,\omega_r\sin\Delta\varphi_t\sin(\theta+\varphi_{\text{LPF}})] \\ u_{\beta l\_t} = \frac{U_h}{2}[2\omega_{ex}\cos\Delta\varphi_t\sin(\theta+\varphi_{\text{LPF}}) \\ \qquad +\,\omega_r\sin\Delta\varphi_t\cos(\theta+\varphi_{\text{LPF}})] \end{cases} \tag{8}$$

where φ_{LPF} is the phase shift caused by the LPF.

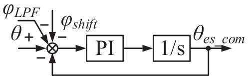

Fig. 6. Simplified schematic diagram of the compensation method.

Then, the rotor position error signal obtained in PLL can be expressed as

$$f(\Delta\theta)_{\_t} = \frac{U_h}{2}\left[\underbrace{2\omega_{ex}\cos\Delta\varphi_t\sin(\Delta\theta_{\_t}+\varphi_{LPF})}_{\text{position error component}} + \underbrace{\omega_r\sin\Delta\varphi_t\cos(\Delta\theta_{\_t}+\varphi_{LPF})}_{\text{interference component}}\right] \tag{9}$$

where $\Delta\theta_{\_t} = \theta - \theta_{es\_t}$ is the error between the actual rotor position and the estimated rotor position, θ_{es_t} is the estimated rotor position. It can be seen from (9) that in addition to the rotor position error component, the input signal of PI controller also contains the interference component caused by the phase difference between the demodulation signal and the HF response signals, and it also increases the difficulty in adjusting the phase-locked parameters.

Then, the estimated rotor position with the consideration of the errors above can be expressed as

$$\theta_{es\_t} = \theta + \varphi_{\text{shift}} + \varphi_{\text{LPF}} \tag{10}$$

where φ_{shift} is the phase-shift caused by the interference component in (9), and it increases with the rotational speed rising. Thus, the compensation should be added to the heterodyne demodulation module. The simplified schematic diagram of the compensation method is shown in Fig. 6, where θ_{es_com} is the estimated rotor position after compensation. As φ_{shift} increases when $\Delta\varphi_t$ is rising, meanwhile, the SNR of the rotor position error component in (9) is deteriorated. Especially, when $\Delta\varphi_t$ is close to $\pi/2$ or $3\pi/2$, the amplitude of the rotor position error component in (9) is close to 0, and it will lead to the failure of the traditional heterodyne demodulation module.

From the above analysis, it can be observed that both the asynchronous demodulation signal and the LPF in the traditional heterodyne demodulation module increase the rotor position estimation error when the rotational speed increases in the starting procedure, and it even leads to the failure of the rotor position estimation in the extreme case.

C. Synchronous Demodulation Signal Generation

In order to improve the accuracy and reliability of the rotor position estimation scheme for the sensorless starting control of TSSM, a synchronous demodulation signal with the same frequency and phase as the HF response signals is necessary to be generated and employed in the heterodyne demodulation module [27]. As the phase of the HF response signals determined by parameters of TSSM is constant, the synchronous demodulation signal employed for demodulation can be generated at the standstill status. Then, the synchronous demodulation signal generation method based on the field current of ME can be shown in Fig. 7.

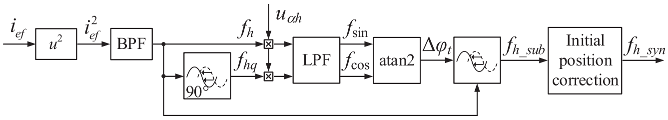

Fig. 7. Schematic diagram of the synchronous demodulation signal generation method based on the field current of ME.

From Fig. 4 and (5), it can be seen that the frequency of the HF response signals is twice that of the ac excitation power. In order to achieve the synchronous demodulation signal, the field current i_{ef} of ME needs to be squared and filtered by the band-pass filter (BPF) to generate f_h whose frequency is the same as that of the HF response signal. Then, f_h and its orthogonal signal f_{hq} are multiplied by the HF response signal in the α-axis separately

$$\begin{cases} u_{\alpha h}\cdot f_h = 2\omega_{ex}U_h\cos(2\omega_{ex}t+\varphi_h) \\ \qquad\qquad \cdot\cos(2\omega_{ex}t+\varphi_{d\_t})\cos\theta_0 \\ \qquad\qquad = \omega_{ex}U_h[\cos(4\omega_{ex}t+\varphi_{\text{sum}})+\cos\Delta\varphi_t]\cos\theta_0 \\ u_{\alpha h}\cdot f_{hq} = 2\omega_{ex}U_h\cos(2\omega_{ex}t+\varphi_h) \\ \qquad\qquad \cdot\sin(2\omega_{ex}t+\varphi_{d\_t})\cos\theta_0 \\ \qquad\qquad = \omega_{ex}U_h[\sin(4\omega_{ex}t+\varphi_{\text{sum}})+\sin\Delta\varphi_t]\cos\theta_0 \end{cases} \tag{11}$$

where θ_0 is the initial rotor position of MG.

The signals $f_{\sin}$ and $f_{\cos}$ in Fig. 7 containing sin$\Delta\varphi_t$ and cos$\Delta\varphi_t$ in (11) can be extracted by LPFs. Then, the phase difference $\Delta\varphi_t$ is obtained by the arctangent function, and the signal f_{h_sub} is obtained by the compensation of $\Delta\varphi_t$. Due to the sign value of θ_0, there may be a phase difference π between the phase of f_{h_sub} and φ_h. Therefore, the synchronous demodulation signal f_{h_syn} is obtained after the initial position correction module [27]

$$f_{h\_\text{syn}} = k_{fh}\cos(2\omega_{ex}t+\varphi_h) \tag{12}$$

where k_{fh} is the amplitude of the synchronous demodulation signal.

As shown in Fig. 7, there are various issues that have side effect on the generation of synchronous demodulation signals. First, the high-precision current sensor is required to sample the field current of ME, which not only increases the cost of the platform, but also has a side effect on the accuracy of the demodulation signal due to the inherent sampling error. Second, the synchronization between the demodulation signal generated and the HF response signals is poor for the reason that the accurate signal delay is difficult to achieve in the discrete digital system. Moreover, since the additional BPF and LPF are necessary in the synchronous demodulation signal generation, the phase calculated in Fig. 7 of the synchronous demodulation signal is distorted by the corresponding phase shift of the filters. Thus, the demodulation method with the properties of less dependence on filters and signals sampled by hardware should be employed for the sensorless starting control of TSSM.

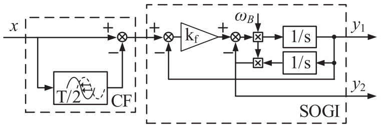

Fig. 8. Schematic diagram of the CF-SOGI cascade filter.

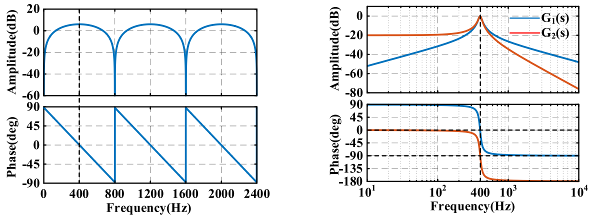

(a) (b)

Fig. 9. Bode diagrams of CF and SOGI. (a) CF. (b) SOGI.

III. Quadrature Signals Synchronous Demodulation Method

A. Quadrature Signals Generation Method

As aforementioned issues of the synchronous demodulation signals, quadrature signals according to the HF response signals in the $\alpha\beta$-axis are extracted and employed to improve the synchronous demodulation scheme, where a cascade filter of comb filter (CF) and the SOGIs as shown in Fig. 8 is adopted herein for the HF response signals extraction and quadrature signals generation.

The transfer function of the CF can be expressed as

$$G_{\text{comb}}(s) = 1 - e^{-\frac{T}{2}s} \tag{13}$$

where T is the period corresponding to the center frequency. The amplitude-frequency and phase-frequency characteristics of CF can be obtained as

$$A_{\text{comb}}(\omega) = |G_{\text{comb}}(j\omega)| = 2\left|\sin\left(\frac{\pi\omega}{2\omega_B}\right)\right| \tag{14}$$

$$\varphi_{\text{comb}}(\omega) = \angle G_{\text{comb}}(j\omega) = \frac{\pi}{2} - \frac{\pi\omega}{2\omega_B} \tag{15}$$

where ω_B is the center frequency of the filter and ω is the frequency of the input signal.

Fig. 9(a) shows the bode diagram of CF, the center frequency is set to 400 Hz, which is twice the excitation frequency, and the HF response signals in (5) could be extracted. As the harmonic distribution shown in Fig. 4, in order to extract the specific second HF response signals, it is necessary to filter out the dc component and periodic harmonics, which are $2k$ ($k = 1,2,3\ldots$) and $2k + 1$ times the center frequency of the CF. The dc component and harmonic signal of 800 Hz should be filtered, and the amplitude of harmonics decreases with the frequency increasing. The amplitude gains of the CF are both zero at the frequency of 0 and 800 Hz as shown in Fig. 9(a) and expression in (14), which means that the harmonic of 400 Hz as the HF response signals can be extracted accurately. Moreover, since the amplitude-frequency characteristic of the CF is periodic, the components of $2k$ times the center frequency can be filtered out effectively. The poor suppression characteristics for harmonics with the frequency of $2k + 1$ times the center frequency of CF are compensated by the SOGI.

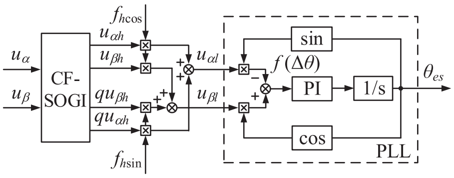

Fig. 10. Schematic diagram of the quadrature signals synchronous demodulation method.

The transfer function of the SOGI can be expressed as

$$\begin{aligned} G_1(s) &= \frac{k_f\omega_B s}{s^2 + k_f\omega_B s + \omega_B^2} \\ G_2(s) &= \frac{k_f\omega_B^2}{s^2 + k_f\omega_B s + \omega_B^2} \end{aligned} \tag{16}$$

where G_1(s) and G_2(s) are the transfer functions corresponding to the output y_1 and y_2 respectively, k_f is the damping coefficient of SOGI, ω_B is the center frequency of SOGI.

The filter characteristics of SOGI are determined by the value of k_f of SOGI, when k_f decreases, the filtering accuracy of SOGI increases, while the dynamic performance of the rotor position estimation system is worse, and it leads to the slow demodulation rate. As a result, k_f is set to 0.1 as shown in Fig. 9(b) with respect to the comprehensive analysis, the amplitude gain of G_1(s) and G_2(s) for the HF harmonics with the frequency of $2k + 1$ times the center frequency of SOGI is below -25 dB, so that the corresponding harmonics could be suppressed effectively. Moreover, since the phase shifts of $G_1(s)$ and $G_2(s)$ at the center frequency are 0° and 90° respectively, the outputs y_1 and y_2 are the quadrature signals.

Then, the quadrature signals extracted by CF-SOGI can be expressed as

$$\begin{cases} u_{\alpha h} = 2U_h[2\omega_{ex}\cos(2\omega_{ex}t + \varphi_h)\cos\theta \\ \qquad\quad -\omega_r\sin(2\omega_{ex}t + \varphi_h)\sin\theta] \\ qu_{\alpha h} = 2U_h[2\omega_{ex}\sin(2\omega_{ex}t + \varphi_h)\cos\theta \\ \qquad\quad +\omega_r\cos(2\omega_{ex}t + \varphi_h)\sin\theta] \\ u_{\beta h} = 2U_h[2\omega_{ex}\cos(2\omega_{ex}t + \varphi_h)\sin\theta \\ \qquad\quad +\omega_r\sin(2\omega_{ex}t + \varphi_h)\cos\theta] \\ qu_{\beta h} = 2U_h[2\omega_{ex}\sin(2\omega_{ex}t + \varphi_h)\sin\theta \\ \qquad\quad -\omega_r\cos(2\omega_{ex}t + \varphi_h)\cos\theta] \end{cases} \tag{17}$$

where $qu_{\alpha h}$ and $qu_{\beta h}$ are the quadrature signals to $u_{\alpha h}$ and $u_{\beta h}$, respectively.

Then, a quadrature signals synchronous demodulation method as shown in Fig. 10 could be adopted for the rotor position estimation. The cascade filter composed of the CF and the SOGIs is employed to extract the HF response signal and generate the corresponding quadrature signals.

The quadrature demodulation signals $f_{h\_\cos}$ and $f_{h\_\sin}$ without the phase adjustment can be expressed as

$$\begin{cases} f_{h\_\cos} = \cos(2\omega_{ex}t + \varphi_d) \\ f_{h\_\sin} = \sin(2\omega_{ex}t + \varphi_d) \end{cases} \tag{18}$$

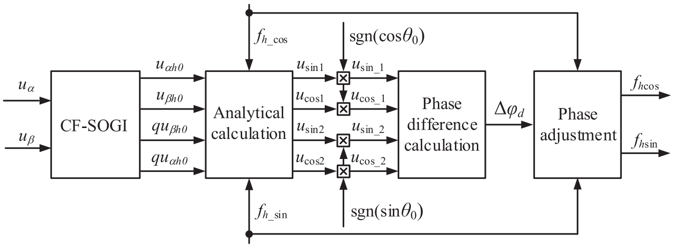

Fig. 11. Schematic diagram of quadrature synchronous demodulation signal generation.

where φ_d is the phase angle of the demodulation signals.

Then, the LF response signals with the rotor position information could be calculated by the product of the synchronous demodulation signals and the HF response signals without LPF, and the corresponding phase shift of the filters could be eliminated.

The rotor position error information input to the PLL by the proposed quadrature signals synchronous demodulation method can be expressed as

$$f(\Delta\theta) = 2U_h\left[\underbrace{1\omega_{ex}\cos\Delta\varphi_d\sin\Delta\theta}_{\text{position error component}} + \underbrace{\omega_r\sin\Delta\varphi_d\cos\Delta\theta}_{\text{interface component}}\right] \tag{19}$$

where $\Delta\varphi_d = \varphi_h - \varphi_d$ is the phase difference between the HF response signals and the demodulation signals, $\Delta\theta = \theta - \theta_{\text{es}}$, θ_{es} is the estimated rotor position of MG.

From (19), there is an interference component caused by $\Delta\varphi_d$ existing in the rotor position error, thus, it can be observed that the generation of an accurate synchronous demodulation signal to eliminate the phase difference $\Delta\varphi_d$ is necessary for the rotor position estimation.

B. Quadrature Signals Synchronous Demodulation Method

Based on the extracted quadrature signals in (17), the schematic diagram of quadrature synchronous demodulation signal generation is shown in Fig. 11, and the simplified phase difference calculation method is also proposed. Compared with the traditional demodulation method shown in Figs. 5 and 7, the signal delay link and additional filters are not used herein, the corresponding phase calculation error could be avoided to simplify the structure.

At the standstill status, the analytical calculation module in Fig. 11 is

$$\begin{cases} u_{\sin 1} = qu_{\alpha h0}\cdot f_{h\_\cos} - u_{\alpha h0}\cdot f_{h\_\sin} \\ \quad = 4U_h\omega_{ex}\sin\Delta\varphi_d\cos\theta_0 \\ u_{\cos 1} = qu_{\alpha h0}\cdot f_{h\_\sin} + u_{\alpha h0}\cdot f_{h\_\cos} \\ \quad = 4U_h\omega_{ex}\cos\Delta\varphi_d\cos\theta_0 \\ u_{\sin 2} = qu_{\beta h0}\cdot f_{h\_\cos} - u_{\beta h0}\cdot f_{h\_\sin} \\ \quad = 4U_h\omega_{ex}\sin\Delta\varphi_d\sin\theta_0 \\ u_{\cos 2} = qu_{\beta h0}\cdot f_{h\_\sin} + u_{\beta h0}\cdot f_{h\_\cos} \\ \quad = 4U_h\omega_{ex}\cos\Delta\varphi_d\sin\theta_0 \end{cases}. \tag{20}$$

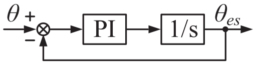

Fig. 12. Simplified PLL schematic diagram in the quadrature signals synchronous demodulation method.

In different sectors, the signs of cosθ_0 and sinθ_0 are different, and it affects the calculation of $\Delta\varphi_d$. Therefore, based on the induced currents of the armature windings of MG during the excitation process, the sign information of cosθ_0 and sinθ_0 can be summarized as

$$\begin{cases} \operatorname{sgn}(\cos\theta_0) = -\operatorname{sgn}(i_\alpha) \\ \operatorname{sgn}(\sin\theta_0) = -\operatorname{sgn}(i_\beta) \end{cases} \tag{21}$$

where i_α and i_β are the armature currents in the $\alpha\beta$-axis of MG, respectively.

Then, the influence of the signs of cosθ_0 and sinθ_0 is eliminated by multiplication, and the (20) can be expressed as

$$\begin{cases} u_{\sin\_1} = 4U_h\omega_{ex}\sin\Delta\varphi_d\,|\cos\theta_0| \\ u_{\cos\_1} = 4U_h\omega_{ex}\cos\Delta\varphi_d\,|\cos\theta_0| \\ u_{\sin\_2} = 4U_h\omega_{ex}\sin\Delta\varphi_d\,|\sin\theta_0| \\ u_{\cos\_2} = 4U_h\omega_{ex}\cos\Delta\varphi_d\,|\sin\theta_0| \end{cases}. \tag{22}$$

It can be seen that both the equation pairs $u_{\sin\_1}$, $u_{\cos\_1}$ and $u_{\sin\_2}$, $u_{\cos\_2}$ can be adopted for the phase difference calculation. In order to improve the SNR for calculation, it is necessary to compare the values of cosθ_0 and sinθ_0, so that the group of signals with larger amplitude in (22) is employed to achieve the phase difference calculation module in Fig. 11 as follows:

$$\Delta\varphi_d = \begin{cases} \arctan\frac{u_{\sin\_1}}{u_{\cos\_1}}, |u_{\alpha h}| \geq |u_{\beta h}| \\ \arctan\frac{u_{\sin\_2}}{u_{\cos\_2}}, |u_{\alpha h}| < |u_{\beta h}| \end{cases}. \tag{23}$$

On the basis of the phase difference calculation result, the quadrature synchronous demodulation signals can be obtained by adjusting the phase in (18) and shown as

$$\begin{cases} f_{h\cos} = \cos(2\omega_{ex}t + \varphi_d + \Delta\varphi_d) = \cos(2\omega_{ex}t + \varphi_h) \\ f_{h\sin} = \sin(2\omega_{ex}t + \varphi_d + \Delta\varphi_d) = \sin(2\omega_{ex}t + \varphi_h) \end{cases}. \tag{24}$$

Then, the rotor position estimation error is obtained by the PLL and expressed as

$$f(\Delta\theta) = 4U_h\omega_{ex}\sin\Delta\theta. \tag{25}$$

The PLL structure of the quadrature signals synchronous demodulation method can be simplified as the schematic diagram shown in Fig. 12. Compared to Fig. 6, as the LPF is replaced by mathematical calculation, the φ_{LPF} is eliminated, and the φ_{shift} is mitigated by the synchronous demodulation method. Therefore, the estimated rotor position θ_{es} will converge to the actual position θ, and it can be used in the sensorless starting control of TSSM.

The schematic diagram of the sensorless starting control strategy for TSSM is shown in Fig. 13, where the field winding of ME is excited by the external single-phase ac power supply, and the $i_d\ = 0$ vector control scheme is employed for the starting

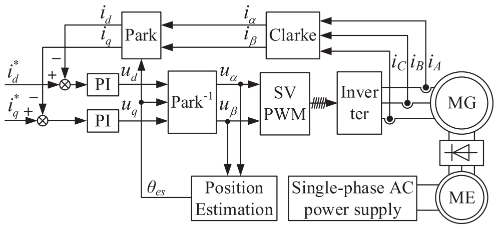

Fig. 13. Schematic diagram of sensorless starting control of TSSM.

TABLE I
PARAMETERS OF THE TSSM

Parameters	Value
Self-inductance of stator of ME	22.2 mH
Resistance of stator of ME	3.7 Ω
Maximum mutual inductance between stator and rotor of ME	2.4 mH
Pole pairs of ME	4
d-axis inductance of MG	0.78 mH
q-axis inductance of MG	1.70 mH
Self-inductance of the rotor of MG	15.9 mH
Resistance of stator of MG	0.032 Ω
Pole pairs of MG	16

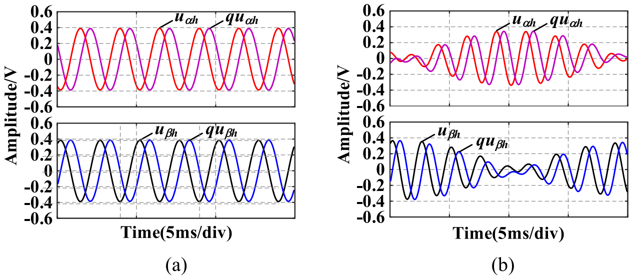

(a) (b)

Fig. 14. Simulation waveforms of quadrature HF response signals. (a) Standstill status. (b) Low-speed range.

control of MG. The voltage signals in the $\alpha\beta$-axis from the output current close-loop controller are employed for the rotor position estimation, and the estimated rotor position is adopted for the coordinate transformation of the vector control for the sensorless starting control of TSSM.

IV. SIMULATION VERIFICATION

To verify the effectiveness of the proposed rotor position estimation method, a simulation model of TSSM is built, the parameters of the prototype of TSSM are shown in Table I. The voltage of the single-phase ac excitation for ME is set to 200 V, and the excitation frequency is 200 Hz, which is determined by the parameters of ME.

The quadrature HF response signals composed of rotor position information extracted by the proposed CF-SOGI cascade filter are shown in Fig. 14. The frequency of the HF response signals is 400 Hz, which is twice the excitation frequency. $u_{\alpha h}$, $qu_{\alpha h}$, and $u_{\beta h}$, $qu_{\beta h}$ are respectively orthogonal to each other. At the standstill status, the amplitude of the HF response signals is fixed, and the ME works as the transformer. While, in the low-speed range, since $2\omega_{ex} >> \omega_r$, the right part in (17) with respect to the rotor speed ω_r could be ignored. As shown in Fig. 14(b), there are two components in the curve according to (17), the HF component is the response 400 Hz HF signal, which is similar to that in Fig. 14(a), while with the rotor rotating, the amplitude of the response HF signal varies according to the rotor position, and the envelope of the curve is a low-frequency component, which indicates the rotor position information.

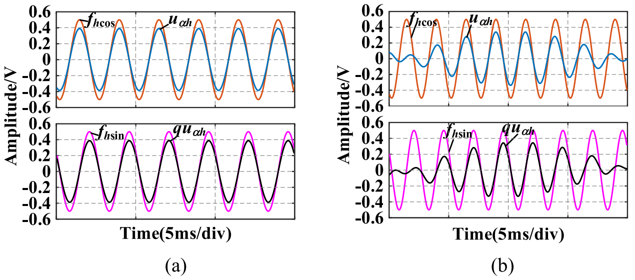

(a) (b)

Fig. 15. Simulation waveforms of synchronous demodulation signals and α-axis HF response signals. (a) Standstill status. (b) Low-speed range.

The waveforms of the generated quadrature synchronous demodulation signals and the HF quadrature response signals in the α-axis are shown in Fig. 15, in the standstill status, the value of cosθ is constant and ω_r is zero, the response signals in (17) are in the same frequency and phase as the demodulation signals in (24). In the low-speed range, since the part with respect to the rotor speed ω_r in (17) is relatively small, in the high-value range of the response signals, it could be neglected, and the quadrature synchronous demodulation signals have the same phase and frequency as the response signals, while, the response signals are deteriorated by the part with respect to the rotor speed ω_r in (17) in the low-value range, however, it almost has no effect on the quadrature synchronous demodulation scheme, and it verifies the effectiveness of the proposed synchronous demodulation signals generation method.

Fig. 16 shows the waveforms of the rotor position estimation error when $\Delta\varphi_d$ is 0, π/4, and $-\pi$/4 at rotational speeds of 50 and 100 r/min. It can be seen from Fig. 16(a) and (b) that when the demodulation signals are synchronized with the HF response signals, there is no steady-state error in the rotor position estimation error at steady state. As the amplitude of the interference component in (19) rises with the rising of the rotational speed, the rotor position estimation error at 100 r/min is larger than that at 50 r/min. In addition, the sign value of the rotor position estimation error varies with the sign value of $\Delta\varphi_d$, which is in good accordance with the characteristic shown in (19).

V. EXPERIMENTAL RESULTS

In order to verify the effectiveness of the aforementioned theoretical and simulation analysis, the experiment platform is implemented based on the digital signal processor (DSP) and the complex programmable logic device (CPLD) as shown in Fig. 17. The sensorless starting control algorithm is achieved by the DSP, and the fault protection is implemented by the CPLD.

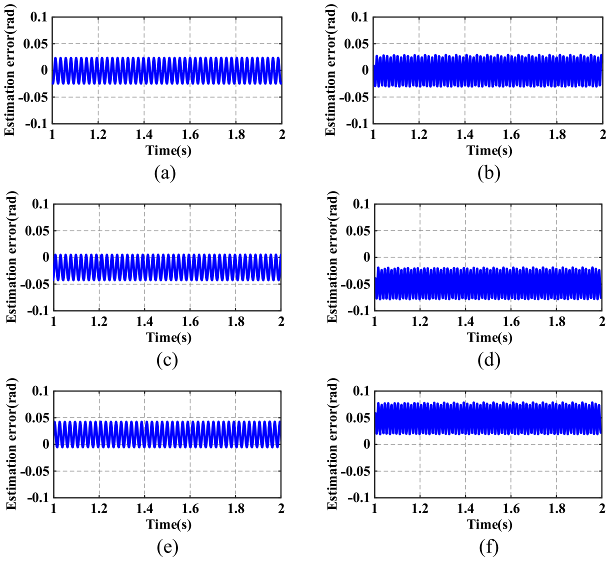

(a) (b) (c) (d) (e) (f)

Fig. 16. Simulation waveforms of position estimation error at different rotational speeds and different $\Delta\varphi_d$. (a) 50 r/min, $\Delta\varphi_d = 0$. (b) 100 r/min, $\Delta\varphi_d = 0$. (c) 50 r/min, $\Delta\varphi_d = \pi/4$. (d) 100 r/min, $\Delta\varphi_d = \pi/4$. (e) 50 r/min, $\Delta\varphi_d = -\pi/4$. (f) 100 r/min, $\Delta\varphi_d = -\pi/4$.

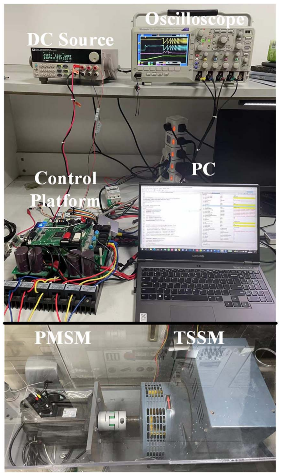

Fig. 17. Experiment platform of the sensorless starting control of TSSM.

A PMSM is coaxially connected to TSSM as a simulated load. The incremental encoder is installed on the side of the PMSM to obtain the actual rotor position as the benchmark, and the accuracy of the rotor position estimation is evaluated by the comparison between the actual rotor position and the estimated rotor position obtained by the proposed method. The parameters of TSSM are the same as that given in Table I. The excitation voltage of ME is set as 200 V, and the excitation frequency is also 200 Hz. The $i_d = 0$ vector control scheme is employed for the sensorless starting control of TSSM, although the speed range is from standstill to 100 r/min, the corresponding fundamental frequency of the MG is 26.7 Hz due to the 16 pole-pairs of the rotor. The specific operating conditions of TSSM at the speed of 0, 50 r/min, and 100 r/min are adopted to verify the proposed quadrature signals synchronous demodulation method as follows.

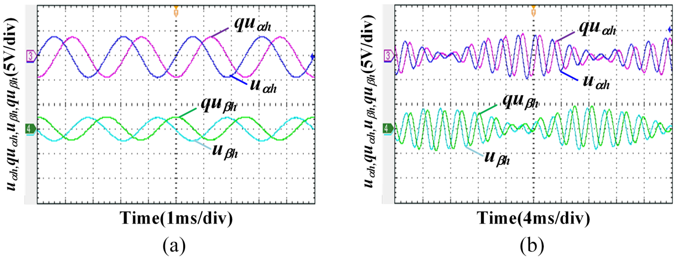

(a) (b)

Fig. 18. Experimental waveforms of quadrature HF response signals. (a) Standstill status. (b) Low-speed range.

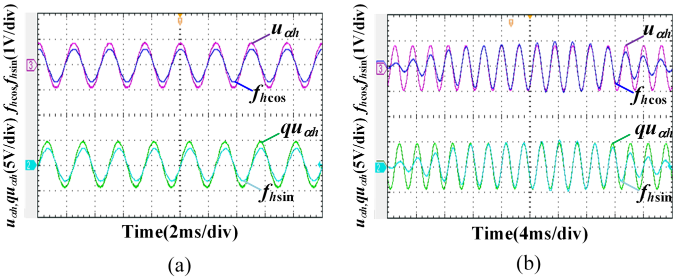

(a) (b)

Fig. 19. Experimental waveforms of synchronous demodulation signals and α-axis HF response signals. (a) Standstill status. (b) Low-speed range.

The experimental waveforms of the HF response signals extracted at the standstill status and low-speed range are shown in Fig. 18, where the dc component and the harmonic components is effectively filtered out by the CF-SOGI, and the quadrature HF response signals containing the rotor position information are generated at the standstill status as shown in Fig. 18(a), at the low-speed of 50 r/min, although the amplitude of the HF response signals varies according to the rotor position, the quadrature HF response signals with slight phase error could also be obtained. The generated synchronous demodulation signals and the HF response signals of α-axis are shown in Fig. 19, and they have the same frequency and phase both at the standstill status. With the speed increasing in the starting procedure, the phase of generated synchronous demodulation signals is in good accordance with that of the HF response signals, and it verifies the effectiveness of the synchronous demodulation signals generation for the rotor position estimation.

The waveforms of the rotor position estimation error at different rotational speeds with different values of $\Delta\varphi_d$ are shown in Fig. 20. When the demodulation signals are synchronized with the HF response signals, the rotor position estimation error is less than 0.08 rad, and the rotational speed almost has no effect on the rotor position estimation error. However, when the demodulation signals are asynchronous to the HF response signals with the absolute phase-shift of $\pi/8$ and $\pi/4$, the rotor position estimation error varies according to the sign value of $\Delta\varphi_d$, and it can be observed that the error rises with the increasing of the phase difference and the rotational speed.

The trend diagram of the rotor position estimation error with different $\Delta\varphi_d$ is summarized and shown in Fig. 21. With the increasing of $\Delta\varphi_d$, when the absolute value of $\Delta\varphi_d$ is less than $\pi/4$, the growth of the estimation error conforms to the

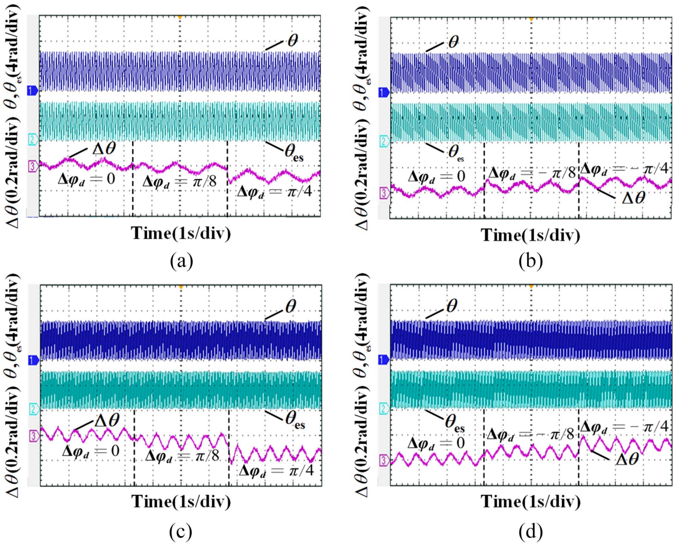

Fig. 20. Experimental waveforms of rotor position estimation error with respect to $\Delta\varphi_d$ at the different speeds. (a) 50 r/min, $\Delta\varphi_d > 0$. (b) 50 r/min, $\Delta\varphi_d < 0$. (c) 100 r/min, $\Delta\varphi_d > 0$. (d) 100 r/min, $\Delta\varphi_d < 0$.

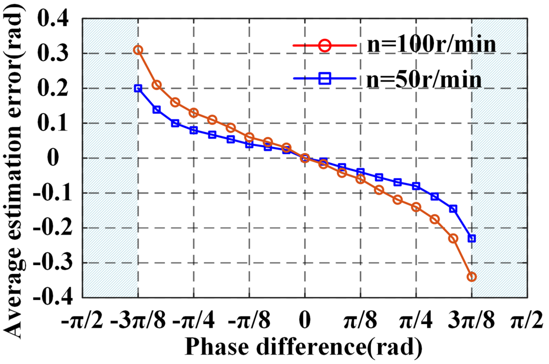

Fig. 21. Trend diagram of the rotor position estimation error with different $\Delta\varphi_d$.

variation trend of the interference component in (19), and it is consistent with $\sin\Delta\varphi_d$. When the absolute value of $\Delta\varphi_d$ is greater than $\pi/4$, the rotor position estimation error grows faster from 0.1 rad. When the absolute value of $\Delta\varphi_d$ is larger than $3\pi/8$, the SNR of the rotor position error component is too low to achieve theoretical PLL for the rotor position estimation due to the large amplitude of the interference component in (19), and rotor position estimation error at 50 r/min is higher than 0.2 rad, while, the error will be higher than 0.3 rad at 100 r/min, then, it will lead to the failure of the rotor position estimation for the sensorless starting control of TSSM.

Fig. 22 shows the experimental waveforms of the actual rotor position θ, the estimated rotor position θ_{es}, and the rotor position estimation error $\Delta\theta$ during the starting process from initial to 50 r/min with different $\Delta\varphi_d$. In the initial stage of the starting procedure, due to the large acceleration ratio, there is a relatively large positive rotor estimation error compared to that in the steady state, and it is almost the maximum value of 0.2 rad in the starting procedure, which is not related to the values of $\Delta\varphi_d$. As it is only located in the initial status of the starting procedure, and the error could also be controlled, it has a slight effect on the sensorless starting control of TSSM. As shown in Fig. 22(a), when the demodulation signal is synchronous with the HF response signals, there is almost no steady-state error in the rotor position estimation error, which could be less than 0.08 rad. However, when the demodulation signal is asynchronous to the HF response signals with the phase-shift of $\pi/4$, as shown in Fig. 22(b) and (c), the steady-state error with respect to the different sign values of $\Delta\varphi_d$ is introduced into the rotor position estimation error, and it rises with the increasing of the rotation speed. It can be seen that the rotor position estimation error could be increased to about 0.2 rad at the speed of 50 r/min.

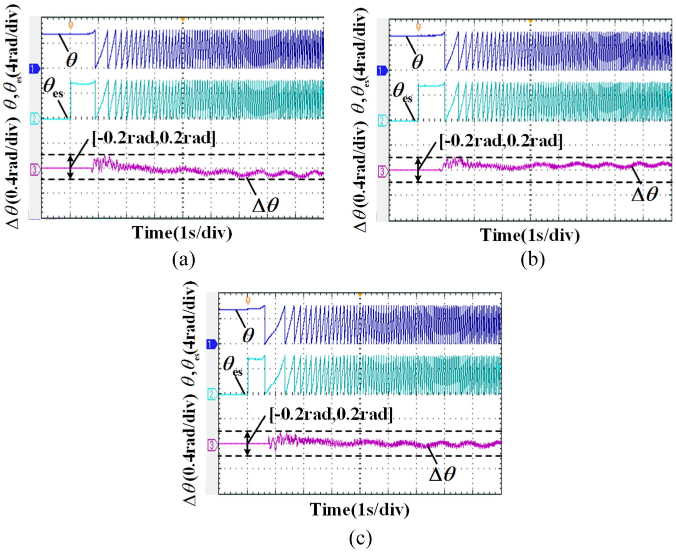

Fig. 22. Experimental waveforms of the starting process with different $\Delta\varphi_d$. (a) $\Delta\varphi_d = 0$. (b) $\Delta\varphi_d = \pi/4$. (c) $\Delta\varphi_d = -\pi/4$.

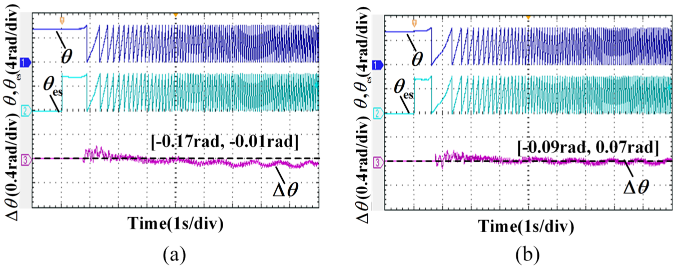

Fig. 23. Comparison results of the different synchronous demodulation strategies. (a) Traditional synchronousdemodulation scheme. (b) Quadrature signals synchronous demodulation method.

Moreover, the comparison results of the traditional synchronous demodulation scheme and the proposed quadrature signals synchronous demodulation method have been implemented and shown in Fig. 23, the phase error of the demodulation signals in the traditional synchronous demodulation scheme will lead to the large rotor position estimation error, and the maximum estimated rotor position error is 0.17 rad as shown in Fig. 23(a), and it will deteriorate the starting performance of TSSM as the increasing of the rotation speed. With the quadrature signals synchronous demodulation method, not only more accurate rotor position estimation could be obtained as shown in Fig. 23(b), but also more stable rotor position error with no relation to the rotation speed could be achieved at the low-speed range, so that the output performance of TSSM in the starting procedure can be improved for the effective cranking of the engine.

VI. Conclusion

In order to overcome the issues of traditional rotor position estimation methods for sensorless starting control of TSSM, the novel quadrature signals synchronous demodulation method based on the HF harmonic self-injection is proposed in this article. The field winding of ME is excited by a single-phase ac source with constant voltage and frequency, the second harmonic generated by the rotary rectifier is used as the HF harmonic signal injected into the field winding of MG indirectly to eliminate the extra injection of HF signal. The generation of the demodulation signal and the function of synchronous demodulation for rotor position estimation can be realized simultaneously by the demodulation structure composed of CF-SOGI cascade filter and pure mathematical logic calculation, the dc bias error and LPF phase-shift error of rotor position estimation caused by heterodyne demodulation structure could be eliminated. The feasibility of the proposed rotor position estimation method of TSSM is finally verified by simulation and experimental results, and the constant rotor position error pulsation is less than 0.08 rad during the starting process, it can be seen that the proposed method has high accuracy and good reliability, and the quadrature signals synchronous demodulation method based on HF harmonic self-injection has good application prospect for the sensorless starting control of TSSM.

References

[1] B. Sarlioglu and C. T. Morris, "More electric aircraft: Review, challenges, and opportunities for commercial transport aircraft," *IEEE Trans. Transp. Electrific.*, vol. 1, no. 1, pp. 54–64, Jun. 2015.

[2] V. Madonna, P. Giangrande, and M. Galea, "Electrical power generation in aircraft: Review, challenges, and opportunities," *IEEE Trans. Transp. Electrific.*, vol. 4, no. 3, pp. 646–659, Sep. 2018.

[3] J. K. Nøland, M. Leandro, J. A. Suul, and M. Molinas, "High-power machines and starter-generator topologies for more electric aircraft: A technology outlook," *IEEE Access*, vol. 8, pp. 130104–130123, 2020.

[4] N. Jiao, Z. Li, S. Mao, C. Sun, and W. Liu, "Aircraft brushless wound-rotor synchronous starter–Generator: A technology review," *IEEE Trans. Power Electron.*, vol. 38, no. 6, pp. 7558–7574, Jun. 2023.

[5] J. Li, Z. Zhang, J. Lu, H. Li, and Z. Chen, "Investigation and analysis of a new shaded-pole main exciter for aircraft starter–Generator," *IEEE Trans. Magn.*, vol. 53, no. 11, Nov. 2017, Art. no. 8209604.

[6] D. Liang, J. Li, and R. Qu, "Sensorless control of permanent magnet synchronous machine based on second-order sliding-mode observer with online resistance estimation," *IEEE Trans. Ind. Appl.*, vol. 53, no. 4, pp. 3672–3682, Jul./Aug. 2017.

[7] F. Jiang et al., "Robustness improvement of model-based sensorless SPMSM drivers based on an adaptive extended State observer and an enhanced quadrature PLL," *IEEE Trans. Power Electron.*, vol. 36, no. 4, pp. 4802–4814, Apr. 2021.

[8] A. Apte, V. A. Joshi, H. Mehta, and R. Walambe, "Disturbance-observer-based sensorless control of PMSM using integral State feedback controller," *IEEE Trans. Power Electron.*, vol. 35, no. 6, pp. 6082–6090, Jun. 2020.

[9] H. Yang, R. Yang, W. Hu, and Z. Huang, "FPGA-based sensorless speed control of PMSM using enhanced performance controller based on the reduced-order EKF," *IEEE J. Emerg. Sel. Topics Power Electron.*, vol. 9, no. 1, pp. 289–301, Feb. 2021.

[10] X. Wu et al., "Improved position observer using adaptive training control-based filter for interior permanent magnet synchronous motor drives," *IEEE Trans. Power Electron.*, vol. 38, no. 8, pp. 10128–10137, Aug. 2023.

[11] A. T. Woldegiorgis, X. Ge, H. Wang, and Y. Zuo, "An active flux estimation in the estimated reference frame for sensorless control of IPMSM," *IEEE Trans. Power Electron.*, vol. 37, no. 8, pp. 9047–9060, Aug. 2022.

[12] A. Griffo, D. Drury, T. Sawata, and P. H. Mellor, "Sensorless starting of a wound-field synchronous starter/generator for aerospace applications," *IEEE Trans. Ind. Electron.*, vol. 59, no. 9, pp. 3579–3587, Sep. 2012.

[13] R. Wang, W. Liu, Y. Zhu, J. Peng, and T. Meng, "A novel initial rotor position estimation method for wound-rotor synchronous starter/generator," in *Proc. IEEE Appl. Power Electron. Conf. Expo.*, 2018, pp. 2440–2445.

[14] R. Wang, W. Liu, T. Meng, and C. Sun, "Fault-tolerant control of position sensor for wound-rotor synchronous starter/generator," in *Proc. 22nd Int. Conf. Elect. Mach. Syst.*, 2019, pp. 1–6.

[15] A. Maalouf, S. Le Ballois, E. Monmasson, J. Midy, and C. Bruzy, "FPGA-based sensorless control of brushless synchronous starter generator at standstill and low speed using high frequency signal injection for an aircraft application," in *Proc. 37th Annu. Conf. IEEE Ind. Electron. Soc.*, 2011, pp. 4003–4008.

[16] T. Meng, W. Liu, N. Jiao, X. Han, R. Wang, and Y. Jiang, "Rotor position estimation for aviation three-stage starter/generators in the low-speed region without high-frequency signal injection," *IEEE Trans. Power Electron.*, vol. 35, no. 8, pp. 8405–8416, Aug. 2020.

[17] X. Zhang, N. Jiao, S. Mao, W. Liu, J. Pang, and Y. Zhou, "Rotor position estimation based on low-frequency signal injection and estimated main field current for wound-field synchronous starter/generator in the low-speed region," *IEEE Trans. Power Electron.*, vol. 38, no. 9, pp. 10869–10879, Sep. 2023.

[18] H. Xue, J. Wei, Z. Zhang, and B. Zhou, "Frequency characteristics of indirect high Frequency signal injection method for sensorless starting control of aircraft starter-generator," in *Proc. IEEE Int. Conf. Elect. Syst. Aircr., Railway, Ship Propulsion Road Veh. Int. Transp. Electrific. Conf.*, 2018, pp. 1–7.

[19] X. Zhang, N. Jiao, S. Mao, W. Liu, D. Zhang, and J. Pang, "Sensorless starting control method based on rotor current characteristics of excitation system for a brushless synchronous starter/generator at low speed," *IEEE Trans. Power Electron.*, vol. 38, no. 12, pp. 15893–15903, Dec. 2023.

[20] S. Mao, C. Ma, N. Jiao, and W. Liu, "Sensorless starting control of the brushless synchronous starter/generator based on flux and parameter estimation of the main exciter," *IEEE Trans. Power Electron.*, vol. 39, no. 1, pp. 1174–1183, Jan. 2024, doi: 10.1109/TPEL.2023.3314858.

[21] J. Wei, H. Xu, B. Zhou, Z. Zhang, and C. Gerada, "An integrated method for three-phase AC excitation and high-frequency voltage signal injection for sensorless starting of aircraft starter/generator," *IEEE Trans. Ind. Electron.*, vol. 66, no. 7, pp. 5611–5622, Jul. 2019.

[22] J. Wang, J. Wei, L. Zhang, C. Hu, Z. Zhang, and B. Zhou, "Improved rotor position estimation method for brushless synchronous starter/generator based on field harmonic signals self-injection scheme," *IEEE Trans. Transp. Electrific.*, vol. 9, no. 2, pp. 3375–3385, Jun. 2023.

[23] J. Peng, W. Liu, N. Jiao, T. Meng, Y. Zhu, and Y. Jiang, "Dual-machine injection method-based sensorless starting strategy for wound-rotor synchronous starter/generator," *IEEE Trans. Power Electron.*, vol. 34, no. 12, pp. 12310–12320, Dec. 2019.

[24] J. Wei, H. Xue, B. Zhou, Z. Zhang, and T. Yang, "Rotor position estimation method for brushless synchronous machine based on second-order generated integrator in the starting mode," *IEEE Trans. Ind. Electron.*, vol. 67, no. 7, pp. 6135–6146, Jul. 2020.

[25] J. Wei, H. Lu, H. Xue, Z. Zhang, and B. Zhou, "The rotor position estimation error improved method for sensorless starting control of brushless synchronous machine," *IEEE Trans. Power Electron.*, vol. 35, no. 8, pp. 8384–8395, Aug. 2020.

[26] R. Wang et al., "Rotor position estimation method of brushless electrically excited synchronous starter/generator based on multistage structure," *IEEE Trans. Power Electron.*, vol. 37, no. 1, pp. 364–376, Jan. 2022.

[27] J. Wang, J. Wei, L. Zhang, C. Hu, Z. Zhang, and B. Zhou, "Synchronous demodulation method of rotor position estimation for brushless Synchronous starter/generator using self-harmonic signal injection," *IEEE Trans. Power Electron.*, vol. 38, no. 1, pp. 862–871, Jan. 2023.

Jiadan Wei (Senior Member, IEEE) received the B.S. and Ph.D. degrees in electrical engineering from Nanjing University of Aeronautics and Astronautics (NUAA), Nanjing, China, in 2003 and 2009, respectively.

Since 2009, he has been a Member of the Faculty with the Department of Electrical Engineering, NUAA, where he is currently a Full Professor with the College of Automation Engineering, NUAA. From 2016 to 2017, he was a Visiting Scholar with the Power Electronics, Machine and Control research Group, University of Nottingham, U.K. His research interests include open-winding electric machine and control, sensorless control of electric machine, and integrated motor and battery charger for electric vehicle.

Zhengyou Cai (Graduate Student Member, IEEE) was born in Yancheng, China, in 2000. He received the B.S. degree in electrical engineering in 2021 from Nanjing University of Aeronautics and Astronautics, Nanjing, China, where he is currently working toward the M.S. degree in power electronics and drives.

His research interests include electrical machine structure and sensorless starting control of the three-stage synchronous machine.

Le Zhang was born in Nanjing, China in 1980. He received the B.S., M.S., and Ph.D. degrees in electrical engineering from Nanjing University of Aeronautics and Astronautics, Nanjing, China, in 2002, 2006, and 2012, respectively.

From 2009 to 2015, he engaged in scientific research in government institutions. Since 2016, he has been a Member of the Faculty with the Department of Automation Engineering, Wuxi Taihu University, Wuxi, China, where he is currently an Associate Professor with the College of Intelligent Equipment Engineering. His research involves wind power generation, motor control, and industrial informatization.

Junhao Yu (Student Member, IEEE) was born in Suzhou, China, in 1998. He received the B.S. degree in electrical engineering in 2020 from Nanjing University of Aeronautics and Astronautics, Nanjing, China, where he is currently working toward the M.S. degree in power electronics and drives.

His research interests include sensorless starting control of the three-stage synchronous machine and the permanent magnet synchronous machine.

Zhuoran Zhang (Senior Member, IEEE) received the B.S. degree in measurement engineering and the M.S. and Ph.D. degrees in electrical engineering from Nanjing University of Aeronautics and Astronautics (NUAA), Nanjing, China, in 2000, 2003 and 2009, respectively.

Since 2003, he has been a Member of the Faculty with the Department of Electrical Engineering, NUAA, where he is currently a Full Professor. From 2012 to 2013, he was a Visiting Professor with Wisconsin Electric Machines and Power Electronics Consortium, University of Wisconsin-Madison. His research interests include design and control of permanent magnet machines, hybrid excitation electric machines, doubly salient electric machines for aircraft power, electric vehicles, and renewable energy generation.

Bo Zhou was born in Wenzhou, China, in1961. He received the B.S. degree in electrical engineering from Zhejiang University, Hangzhou, China, in 1983, the M.S. degree in control engineer from Chongqing University, Chongqing, China, in 1986, and the Ph.D. degree in electrical engineering from Nanjing University of Aeronautics and Astronautics (NUAA), Nanjing, China, in 2000.

He is currently a Professor with the College of Automation Engineering, NUAA, and the Director of the Jiangsu Key Laboratory of New Energy Generation and Power Conversion. His research interests include power converter, electrical machine driving systems, and renewable power systems.

Dr. Zhou was the recipient of the State Technological Invention second-class award in 2009, the Geneva International Invention gold award in 2011, and the Defense Technological Invention first prize in 2008.